Size-Line width Relation in Low-Mass Cores

- $\sigma - D$ relation from NH_3, CS, $C^{18}O$

- relation is observed both core-core and line-line (ie within single core)

- CS, $C^{18}O$ sample more extended gas (non-thermal?)
  NH_3 less extended gas (primarily thermal)
  → distinguish between non-thermal & total line width

  adopt $T = 10K$

$$\Delta V_{TOT}^2 = 8\ln 2 \cdot \frac{kT}{m} + \Delta V_{NT}^2$$

$$= \Delta V_{obs}^2 + 8\ln 2\, kT\left(\frac{1}{m} - \frac{1}{M_{obs}}\right)$$

mean mass ↑   mass of molecule observed ↑

- also check effect of star formation

  8 cores with IRAS sources
  6 " without "   "

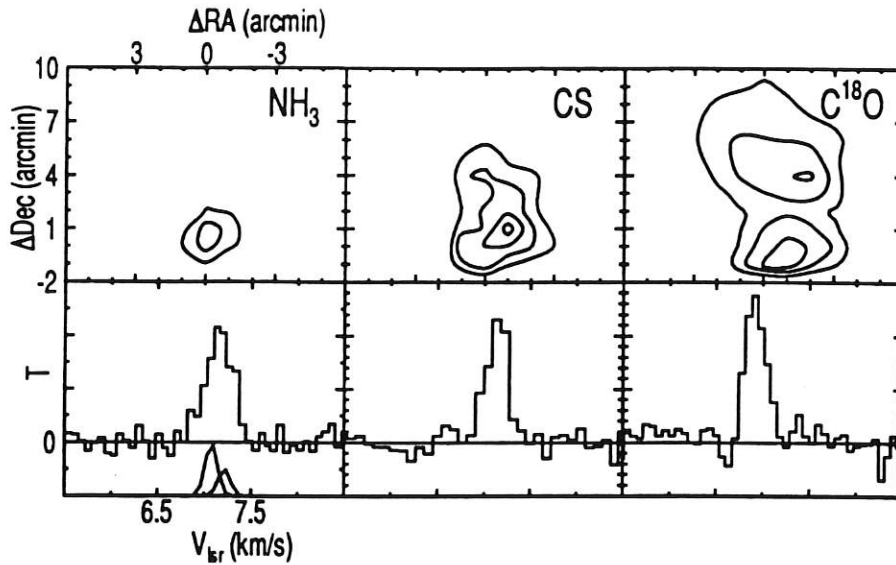 → more scatter for cores with star formation
  → outflows? stellar winds?

Figure 1: The Starless Core L1512. The upper panels show maps of the NH₃ (1,1), CS J= 2 → 1 and C¹⁸O J= 1 → 0 emission from the dense core L1512. The lower panels show the spectra of the emission at the (0,0) position in each map. The NH₃ hyperfine group shown is a blend of two components which are shown by solid line Gaussians below the spectrum. The data are from Benson and Myers (1989) and Fuller (1989).
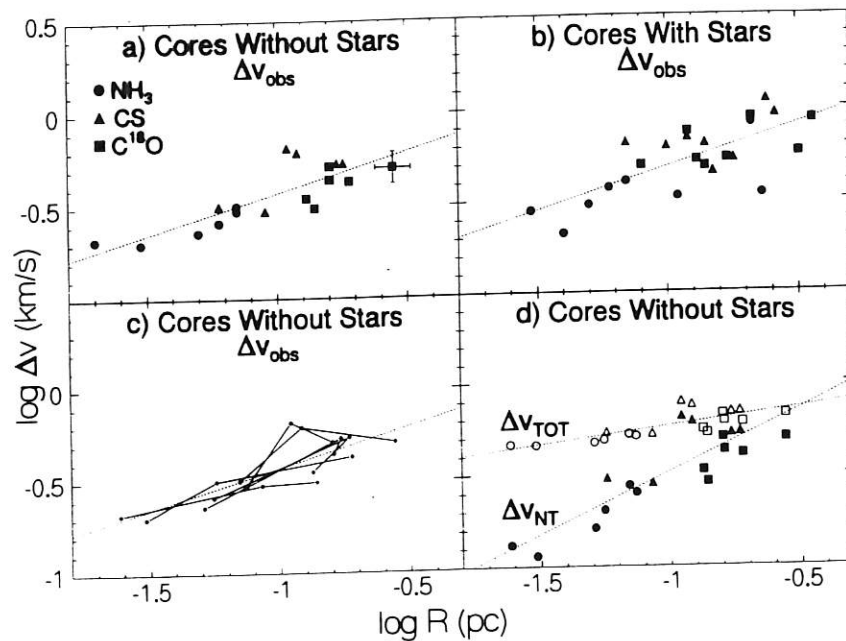
FIG. 1.—The line width–size correlations for the observed cores. The upper panels show the observed line FWHM, Δv_{obs}, vs. size of the emission region, R, for (a) the cores without embedded stars (L1498, L1400G, L1512, L134A, L234A, L63) and (b) cores associated with young stars with luminosities between 0.4 and 15 $L_\odot$ (B5, L1489, L1535, B35, L43B, L255, L1152, L1262A). In each of these two panels the measurements from the C¹⁸O, CS, and NH₃ are shown by different symbols. The broken line in each panel shows the best fit line to the data given in eqs. (1) and (2). The errors bars show the estimated typical uncertainty in the determined size and line width. (c) This panel shows again the data for the starless cores but with the three measurements for each core connected by line segments. The broken line indicates the best-fit line from eq. (1). (d) The variation of the nonthermal component of the observed line widths, Δv_{NT} (filled symbols), and the total velocity width, Δv_{TOT} (open symbols), with size for the starless cores are shown. The shapes of the symbols indicate the molecular tracer as in (a). The broken lines show the correlations given in eqs. (4) and (5).

these cores have less turbulence than most
molecular clouds → linewidths don't reflect
velocity dispersion for mean particle

$$\Delta V_{tot} \propto R^{0.2}$$

$$\Delta V_{NT} \propto R^{0.7}$$

if density is modeled as a single power law
get $\quad n \sim r^{-1.6}$

→ steeper than in outer regions

$$\Delta V_{NT}(r) + n(r) \longrightarrow P_{NT} \propto r^{-0.2}$$

if due to $\vec{B}$ fields, $\quad B \propto r^{-s/2}$

$$s/2 = 0.15 \rightarrow .05$$

→ $\vec{B}$ field strength doesn't vary significantly
over core sizes $\sim 0.02 - 0.25\, pc$

Line Width-Size Relation in Massive Cores

Caselli & Myers 1995, ApJ, 446, 665

Aim: compare massive cores with low-mass cores studied by Fuller & Myers

Sample includes cores in Orion A and Orion B
(avoid regions with large clusters ie NGC 2071)

$\Rightarrow$ 72 cores mapped in at least 2 molecules

new + literature data $\rightarrow$ 24 cores in 3 molecules
(usually CS, NH_3, and ^{13}CO)

Fit ΔV_{NT} vs. R $\rightarrow$ $\Delta V_{NT} \propto R^{0.21}$

(low-mass cores $R^{0.53}$)

$\rightarrow$ massive cores have shallower slope

Also radius at which thermal and non-thermal motions are equal is 15 times smaller for massive cores

$\Rightarrow$ non-thermal motions dominate at all observed size scales

$\Rightarrow$ no significant differences between star-forming and starless cores

Caselli & Myers 1995

Line-width → size relation
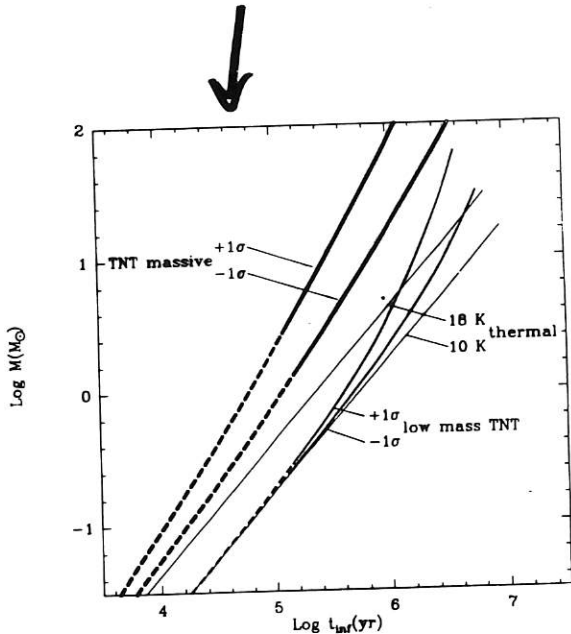
Mass accreted vs. time for TNT models

FIG. 6.—Line width–size relation in (a) *massive* cores in Orion, and (b) *low-mass* cores in Perseus, Taurus, Orion, Ophiuchus, and Cepheus. Dashed lines labeled Δv_T represent the thermal part of the line width of the molecule of mean mass, assuming temperature 18 K (massive cores), or 10 K (low-mass cores). The positions of ammonia cores in these Δv–R diagrams play a crucial role in determining differences between massive and low-mass cores (see text).

FIG. 11.—Accreted stellar mass M as a function of the infall time in massive and low-mass cores. Symbols as in Fig. 9. The lines become dashed to mark the values of the mass enclosed in a sphere of radius equal or less than "R_{min}" where R_{min} indicates the lowest value of the core radius available from observational data (shown in Fig. 6); therefore the dashed part of the diagram represents a numerical extrapolation to the observed physical properties in dense cores. The higher density and pressure in massive cores lead to values for t_{inf} ∼ 6 times shorter than in low-mass cores.
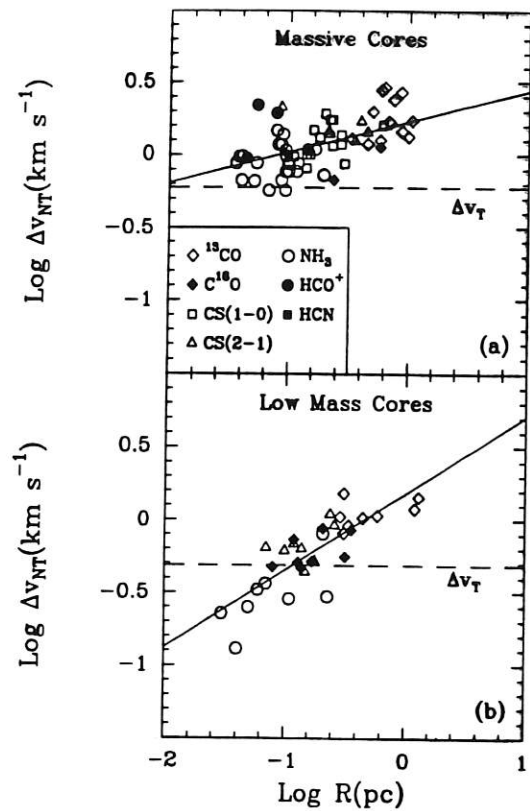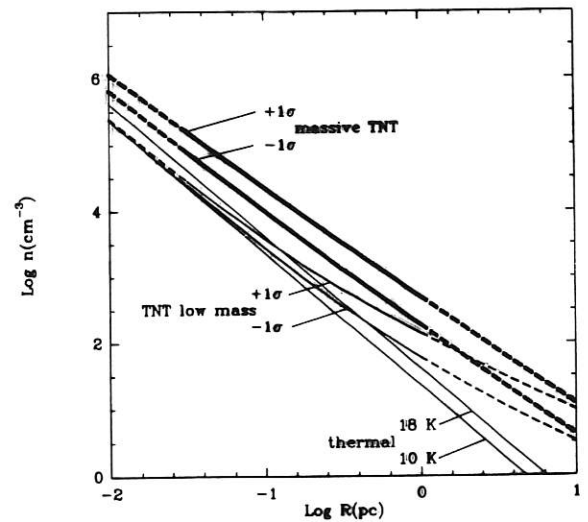

FIG. 9.—Density profiles in massive and low-mass cores obtained from the empirical Δv–R relation, and assuming a spherical symmetric cloud in hydrostatic equilibrium. The dispersion in the calculation of the density profile (lines marked ± 1 σ) reflects the dispersion in the Δv–R relation. The continuous lines trace the density profiles into the size range where the observational data are available (see Fig. 6). The thin lines refer to singular isothermal spheres at 10 and 18 K, where $n(r) \propto r^{-2}$. The nonthermal component of the density profile goes like $r^{-1.6}$ in massive cores and $r^{-1.1}$ in low-mass cores.

density profiles for TNT model

Use model from Myers & Fuller (1992)
→ thermal + non-thermal motions, hydrostatic
 equilibrium

$$\sigma_T = \sigma_{NT} \quad \text{at} \quad r_{TNT}$$

$$\rho \propto r^{-2} \quad \text{for} \quad r \ll r_{TNT} \quad \text{(singular isothermal sphere)}$$

shallower density gradient for $r > r_{TNT}$

Implications for infall:

infall time = time for expansion wave
        to reach position + time to
        collapse from that position

$$t_{exp} = \int_0^x \frac{r_o}{\sigma} dx \qquad x = r/r_o$$

$$t_{coll} = \frac{\pi r^{3/2}}{2 \left[2 G M(<r) \right]^{1/2}}$$

expansion wave travels faster + each layer is denser

⇒ infall times are 6 times shorter in
massive cores than low-mass cores
⇒ massive stars form faster than predicted
by SIS model

Magnetic Fields

- measured from Zeeman splitting in HI, OH, or OH masers
- strengths of order $10-100\mu G$ ↗ in clouds, up to few $1000\mu G$ in massive cores

Line strengths are consistent with magnetic virial equilibrium

$$B_{eq} \approx \frac{3}{8\ln 2}\left(\frac{5}{G}\right)^{1/2}\frac{\Delta v^2}{R}$$

⟹ velocity dispersion is mainly magnetic

Model requires rough equality of magnetic, kinetic, and gravitational energies

or $\quad V_A \approx \Delta V \approx (GM/R)^{1/2}$

Low mass cores have much less magnetic support
→ due to ambipolar diffusion? estimate these cores are just the right size for this to be efficient
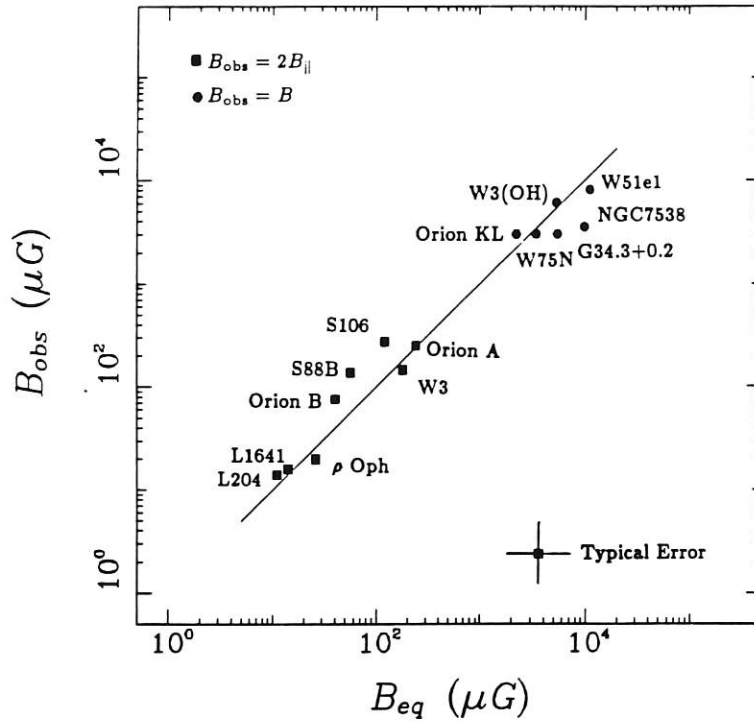
FIG. 1.—Observed and predicted magnetic field strengths in 14 molecular clouds and molecular cloud cores, based on the data in Table 1. The observed field strength B_{obs} is equal to either twice the line-of-sight component, $2B_{\parallel}$ (*filled squares*), or the total field strength, B (*filled circles*). The predicted field strength B_{eq}, from eq. (2), is based on an equilibrium model of a uniform sphere, where the magnetic, kinetic, and gravitational energy density terms of the virial theorem are all equal ($M \approx K \approx G$). The solid line indicates $B_{obs} = B_{eq}$; the error bars indicate estimated uncertainty of a factor of 2.
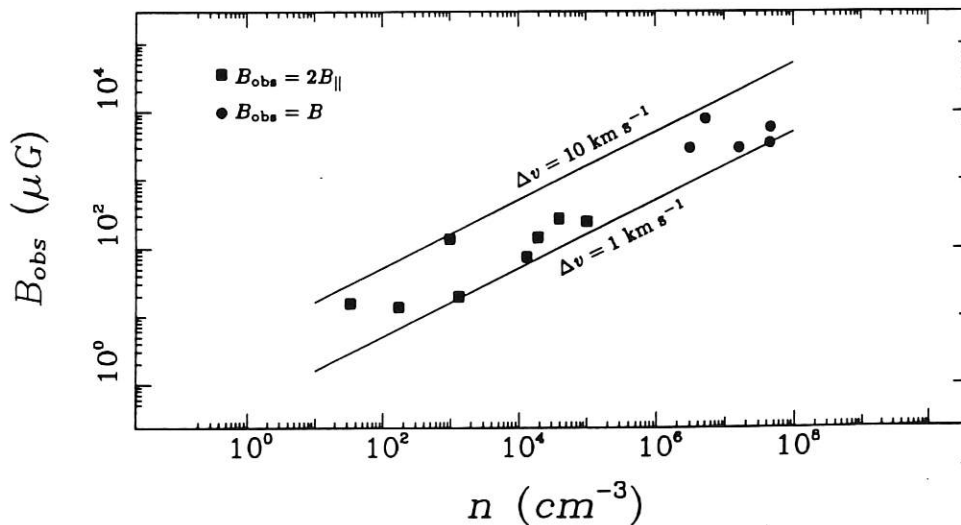

FIG. 2.—Observed magnetic field strength B_{obs} vs. density n based on virial equilibrium ($K \approx G$) for the 14 clouds and cloud cores in Table 1. B_{obs} equals either $2B_{\parallel}$ (*filled squares*) or B (*filled circles*) as in Fig. 1. Solid lines indicate predictions of the equilibrium model, eq. (4), for FWHM line width Δv equal to 1.0, and 10 km s^{-1}.

More on magnetic fields — Crutcher 2010 ARAA

→ 34 Zeeman detections as of 2008

→ $\dfrac{mass}{magnetic\ flux}$ ~ 2 × critical $\left.\phantom{\begin{array}{c}a\\b\\c\end{array}}\right\}$ to within factors of 2

kinetic energy ~ magnetic energy

"super-critical" → $\vec{B}$ field can't support cloud
against collapse

Bayesian model for true magnetic field
strength & its variation with density
→ distribution of observed $B_\parallel = B_z = B_{LOS}$
constrains distribution of B_{tot}

Fit: B_0 ~ 10 μG n_0 ~ 300 cm^{-3} $K = 0.65$

$$B = B_0 (n/n_0)^K \quad for\ n \geq n_0$$
$$= B_0 \quad for\ n < n_0$$

→ suggests clouds become self-gravitating
at n_0 → more isotropic contraction
increases B

→ $K = 0.65$ is significantly steeper than
ambipolar diffusion predicts
→ $\vec{B}$ field too weak to impede contraction
significantly

Figure 1 from Magnetic Fields in Interstellar Clouds from Zeeman Observations: Inference of Total Field Strengths by Bayesian Analysis

Richard M. Crutcher et al. 2010 ApJ 725 466 doi:10.1088/0004-637X/725/1/466
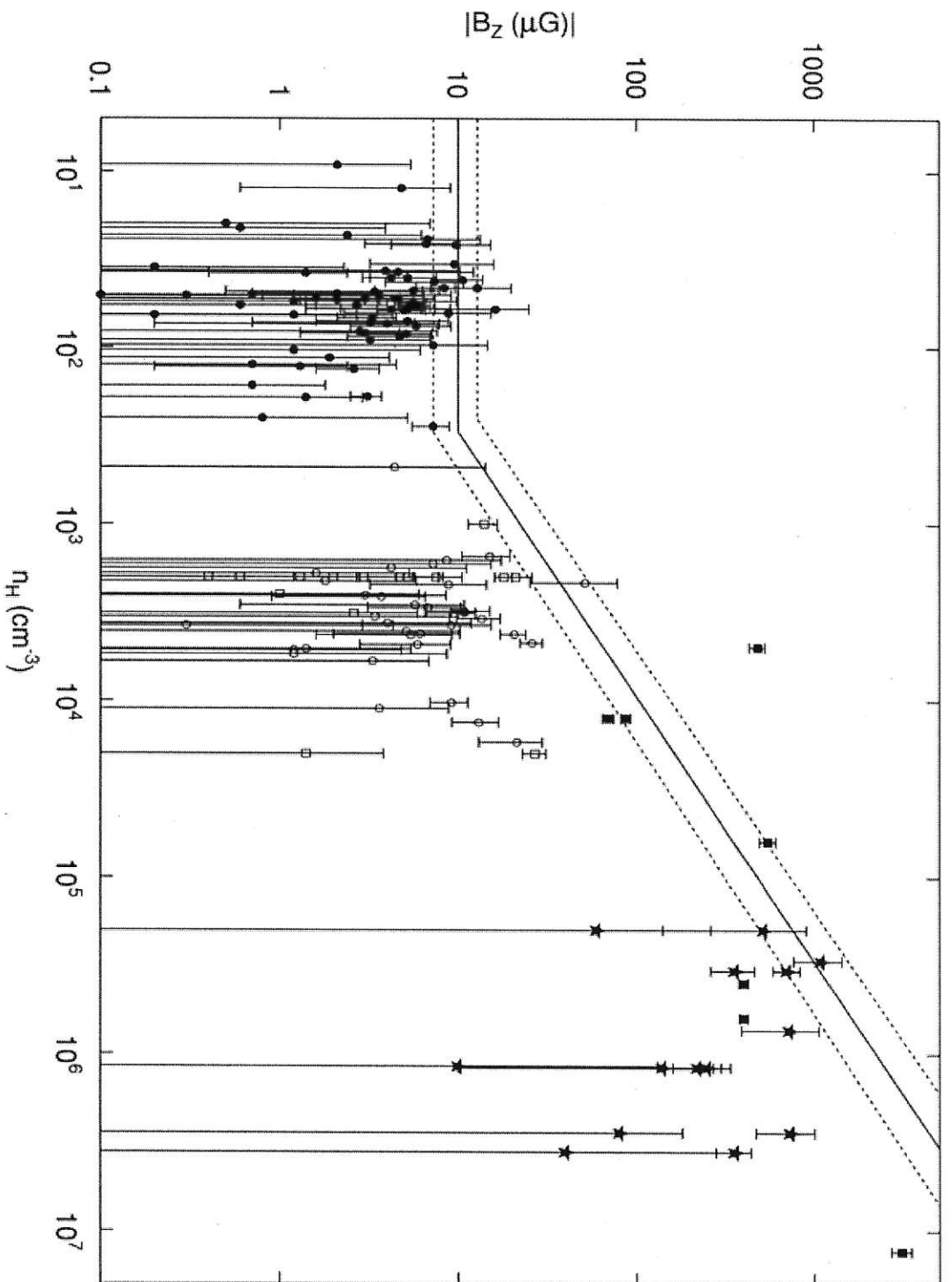
Tracing Small-Scale Magnetic Field Structure in Clouds and Cores

Matthews et al. 2001, ApJ, 562, 400

Matthews & Wilson 2002, ApJ, 574, 822

New instruments since 1997 allow us to study $\vec{B}$ field morphology on scales of 15"
  in highly obscured regions

→ emission from dust grains is polarized
  and traces magnetic field

Limitations

- only trace plane of sky component of magnetic field

- difficult (impossible?) to measure strength of $\vec{B}$ field

- traces average $\vec{B}$ field within the beam
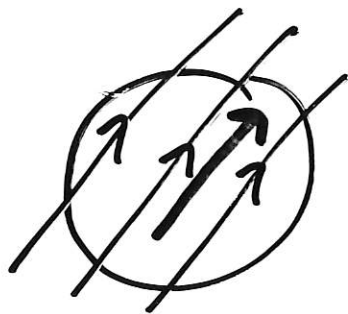
Orion Core OMC 3
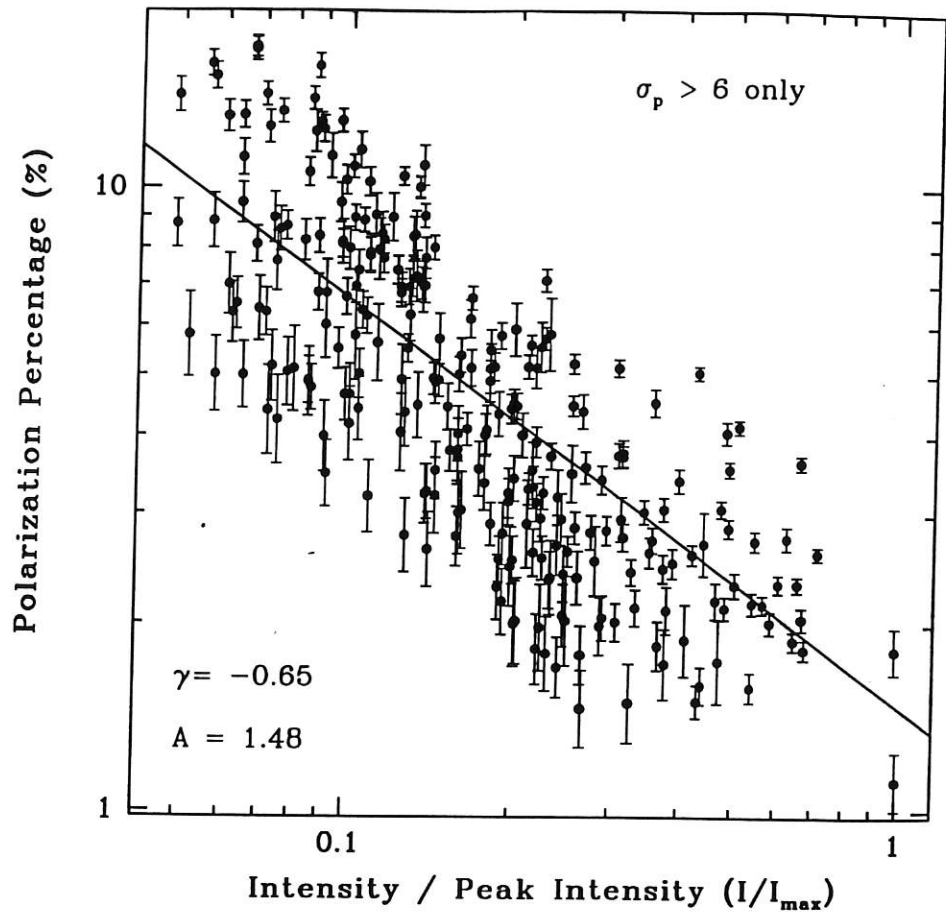
FIG. 4.—Logarithmic plot of polarization percentage vs. intensity (scaled by the maximum intensity point) reveals that higher intensities have systematically lower polarizations. Values plotted are those on Fig. 2, which have $\sigma_p > 6$. The decreasing trend cannot be accounted for by the uncertainties shown here. A χ^2 power-law fit of the form $p = AI^\gamma$ yields the A and γ parameters recorded on the log-log plot. A slope of -0.65 effectively characterizes these data.

Matthews et al.
2001

- polarization percentage is lower where emission is brighter (on filament as well as cores) → feature of filament
→ helical magnetic field?
→ changing grain physics ie with density?
→ $\vec{B}$ fields tangled on scales <15" ?

Barnard 1 dark cloud
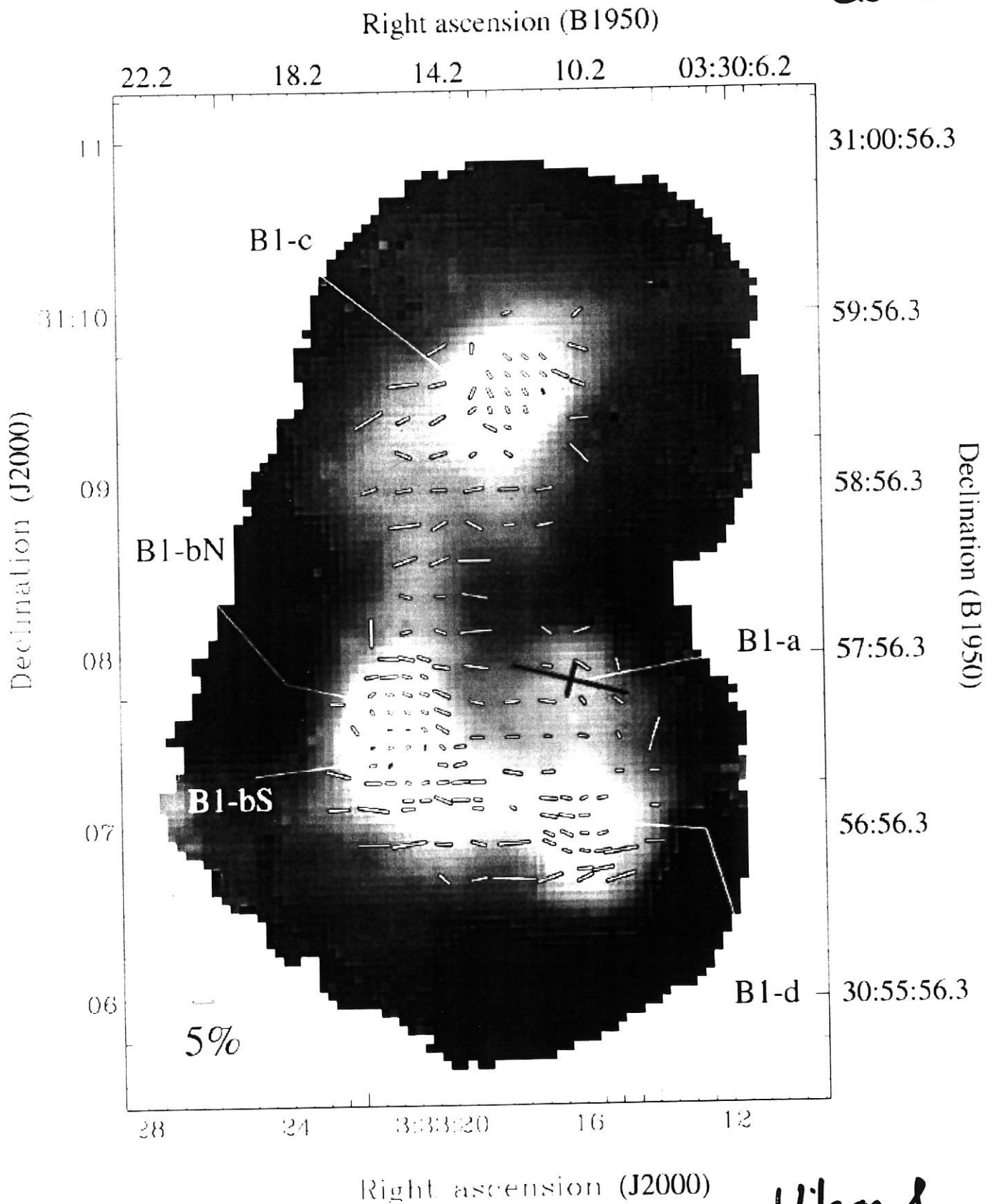
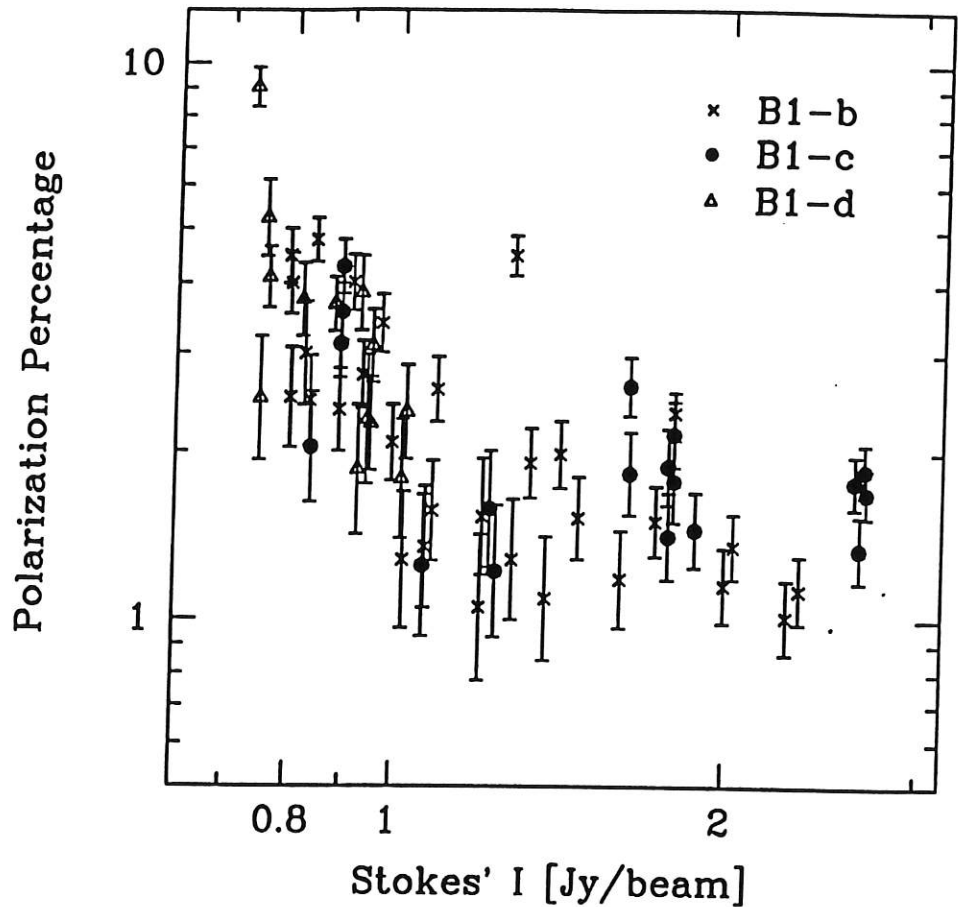Wilson & Matthews 2002

Barnard Cloud B1

FIG. 5.—Depolarization toward individual cores. To better examine the change in polarization percentage at high intensities, we plot $\log p$ vs. $\log I$ for individual cores. Essentially, we take all vectors around each core above the intensity threshold discussed in Fig. 1. By plotting the three bright cores separately, it is clear that B1-b and B1-c show higher values of p than expected given the slope of the relation below 1 Jy beam^{-1}. The threshold corresponds to $\sim$30% of the peak of B1-c and $\sim$40% of B1-b. In the text, we discuss possible systematic effects that could explain this flattening (i.e., the truncation of the data set below 1% and optical depth). We conclude that the threshold is a real effect for the B1-c core.

Matthews &
Wilson 2002

- polarization declines for large I, but reaches a threshold value (unlike Orion)
  → unusual, but no real explanation ...
  → maybe no stars formed yet?
    - but some prestellar cores also exhibit depolarization

Magnetic Fields in B1 Dark Cloud

- polarization vectors are aligned in emission away from bright cores ($\theta \sim 90°$)

- vectors aligned in each core, but angles vary

- no correlation between submm polarization and optical polarization on larger scales

→ estimate total field strength and direction by combining with Zeeman measurements
  - assumes both uniform (B_0) and non-uniform (B_n) components
  - uses dispersion in observed $\vec{B}$ + pol'n

$-B_{0z} = -27 \pm 4 \mu G$; parametrize $\sigma_{Bz}/B_{0z} = .2, .4, .6, .8$

$- \theta_{pol} = 88 \pm 28°$; assume $B_{pos} \perp \theta_{pol}$

→ $B_0 = 31 \mu G \left[\pm (0.52 \hat{N} + 0.01 \hat{E}) - 0.86 \hat{z} \right]$

$\underbrace{\phantom{\pm (0.52 \hat{N} + 0.01 \hat{E})}}_{POS}$ $\underset{LOS}{\uparrow}$

(assuming $\sigma_{Bz}/B_{0z} = 0.2$)
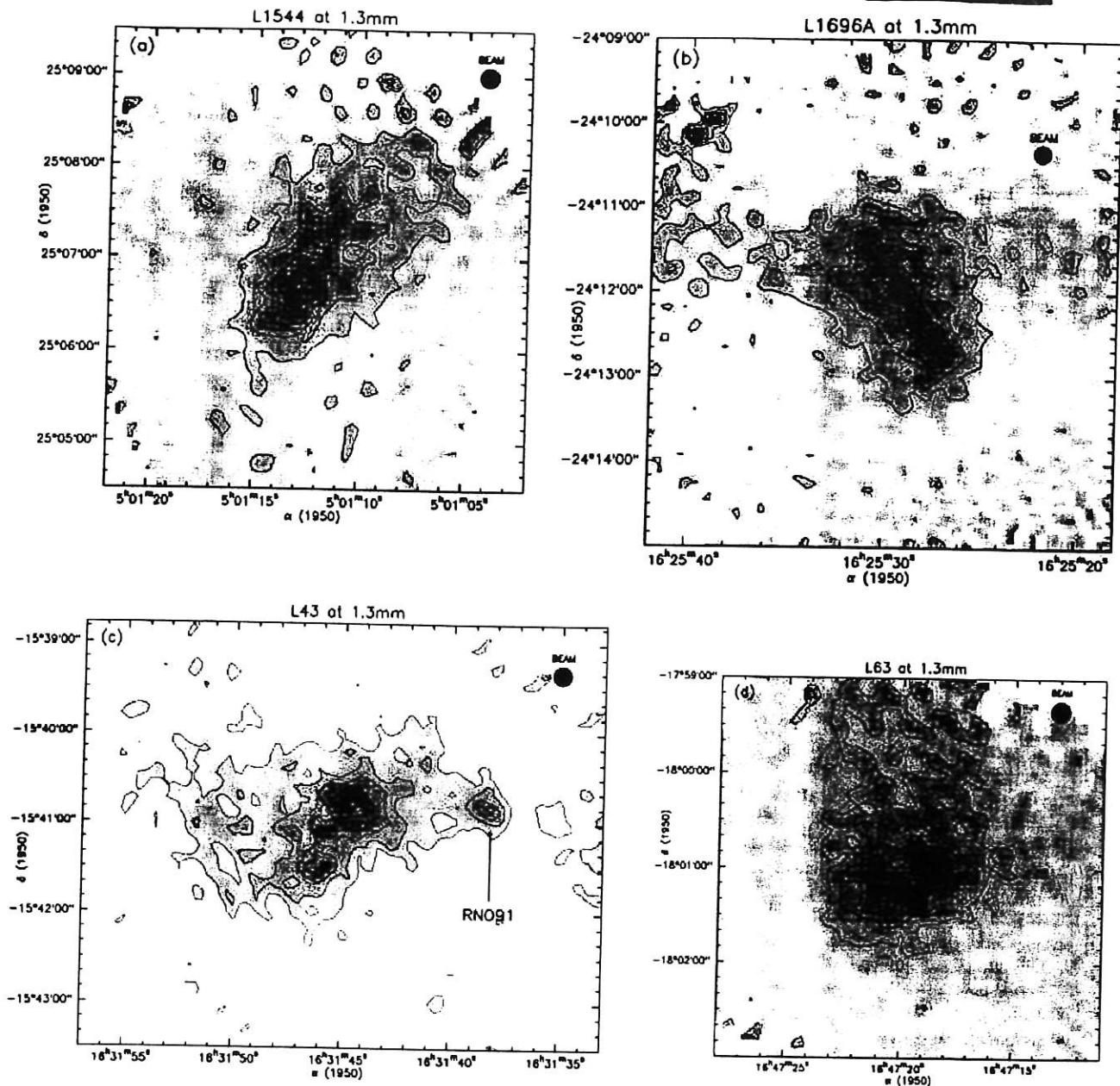
Figure 1. Isophotal contour maps of the 1.3-mm continuum emission from the four pre-stellar cores most clearly detected in the 1.3-mm data, smoothed to a 13-arcsec beam. (a) L1544. Contour levels go from 20 to 80 mJy beam^{-1} in steps of 20 mJy beam^{-1}. The noise level near map centre is ~5 mJy per 13-arcsec beam. (b) L1696A/ρ Oph-D. Contour levels go from 20 to 80 mJy beam^{-1} in steps of 20 mJy beam^{-1}. The noise level near map centre is ~5 mJy per 13-arcsec beam. (c) L43. Contour levels go from 25 to 125 mJy beam^{-1} in increments of 25 mJy beam^{-1}. The noise level near map centre is ~8 mJy per 13-arcsec beam. (d) L63. Contour levels go from 15 to 60 mJy beam^{-1} in steps of 15 mJy beam^{-1}. The noise level near the map centre is ~4 mJy per 13-arcsec beam.

pre-stellar core ≡ gravitationally bound core
                     without a central protostar

• none of these cores is symmetric
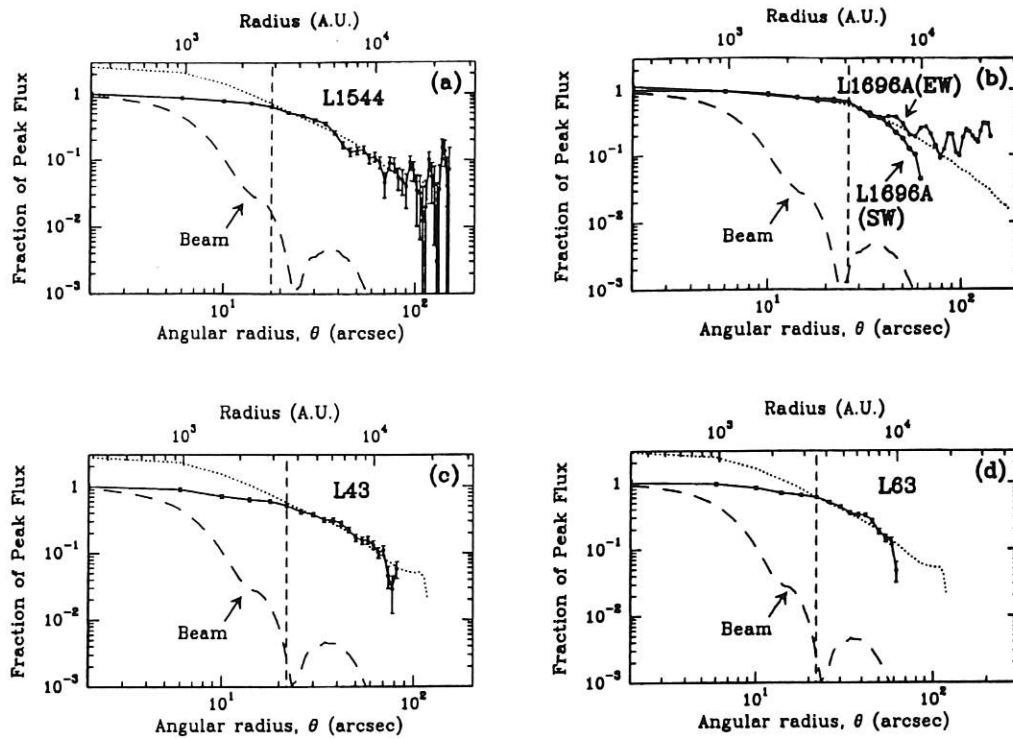• some may have already fragmented

Figure 3. Normalized radial intensity profiles of the four pre-stellar cores from Fig. 1. In each panel the beam profile is shown as a dashed curve, while the dotted line shows a simulated model profile as described in the text. Short-dashed vertical lines mark the radius inside which the inferred density gradients are flatter than $\rho(r) \propto r^{-2}$, which we call R_{flat}. (a) A profile of the circularly averaged south-east quadrant of L1544. (b) An east–west cut of L1696A, averaged along its major axis, compared with the intensity profile obtained by circularly averaging the south-west quadrant of the core. (c) A profile of the circularly averaged north-east quadrant of L43, corresponding to the densest pre-stellar fragment of Fig. 1(c). (d) A profile of the circularly averaged southern part of L63, avoiding emission arising from the filament in the north (see Fig. 1d).

- compare radial flux profiles to what would expect if $\rho \propto r^{-2}$ (singular isothermal sphere)

→ all cores possess a flatter inner region (except maybe L1696A?)
→ not consistent with $\rho \propto r^{-2}$

- profiles are more consistent with equilibrium models like Bonnor-Ebert sphere (or externally heated, self-gravitating thermally supported condensations)
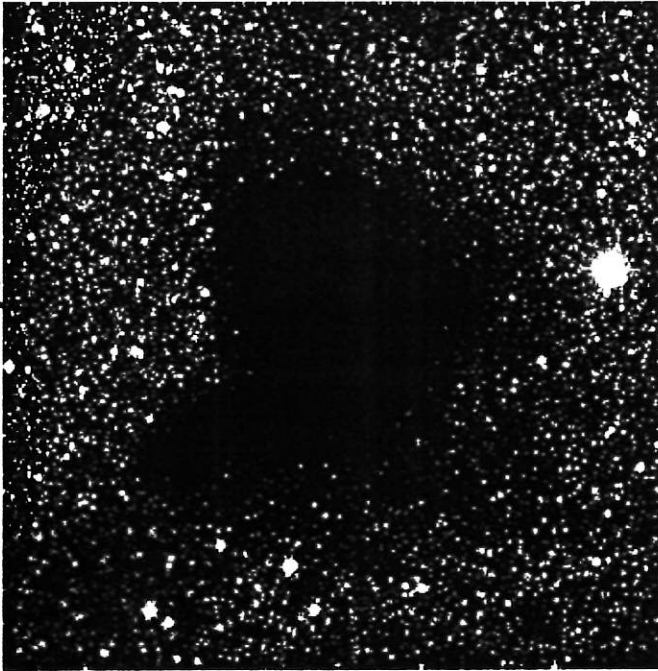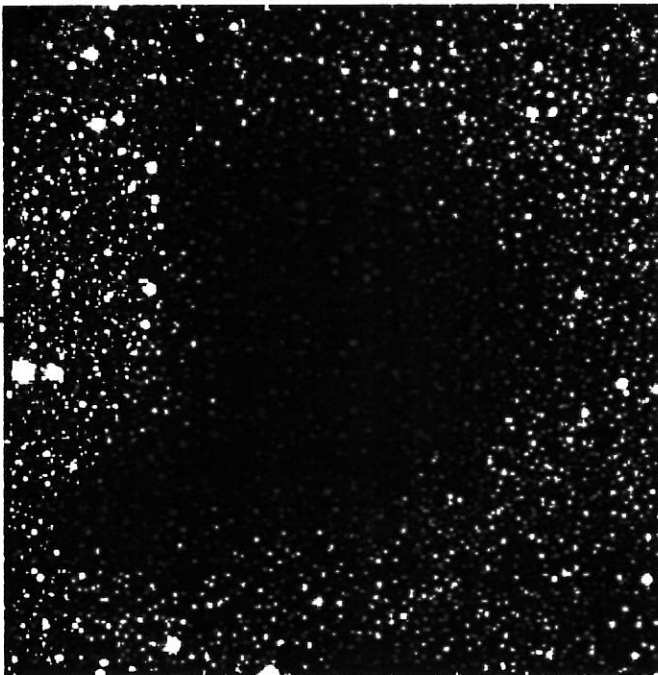
Internal Structure of a Cold Dark Cloud

Close this window to return to the previous window

BVI montage

BIK montage

- determine radial density structure in Barnard 68 directly from extinction of background stars

(most direct density determination as long as gas to dust ratio and extinction law don't vary)

$d = 125 \, pc$

$T = 16 \, K$ (from NH_3)

$M \sim 2 \, M_\odot$

- detect ~1000 stars lying behind cloud

- data give projection on sky of $g(r)$

fit a Bonnor-Ebert sphere to the data

$\rightarrow$ concentration implies just unstable to gravitational collapse

$\Rightarrow$ isothermal, pressure-confined self-gravitating cloud
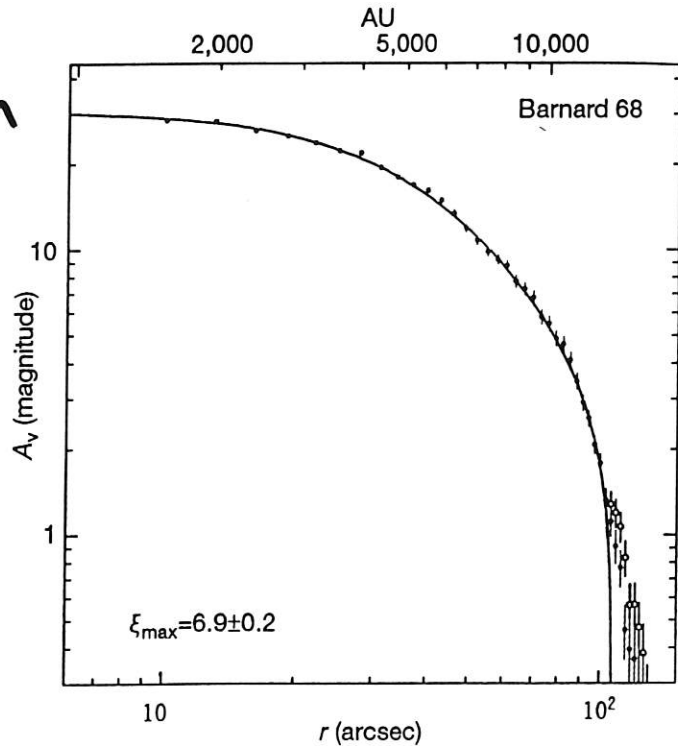
Figure 2 Azimuthally averaged radial dust column density profile of Barnard 68. By convention the dust column density is expressed in terms of magnitudes of visual extinction, A_V. The red circles show the data points for the averaged profile of a sub-sample of the data that do not include the cloud's southeast prominence, seen in Fig. 1. The open circles include this prominence. The error bars were computed as the r.m.s. dispersion of the extinction measurements in each averaging annulus and are smaller than the data points for the central regions of the cloud. The solid line represents the best fit of a theoretical Bonnor–Ebert sphere to the data. The close match of the data with theory indicates that the internal structure of the cloud is well characterized by the equations for a self-gravitating, pressure-confined, isothermal sphere and thus Barnard 68 seems to be a distinct dynamical unit near a state of hydrostatic equilibrium, with gravity balanced by thermal pressure.

Aside: B68 + its 3 neighbors may be left over gas cores from a larger molecular cloud dispelled by massive star formation

$\rightarrow$ might eventually form a small stellar group like TW Hydra

Evans et al. 2001, ApJ, 557, 193

→ self consistent modeling of prestellar cores

Two types of hydrostatic pressure balanced clouds

→ classical isothermal Bonnor-Ebert spheres

→ modified B-E spheres with temperature gradient

include

• radiative transfer code to get T(r)

• vary strength of interstellar radiation field
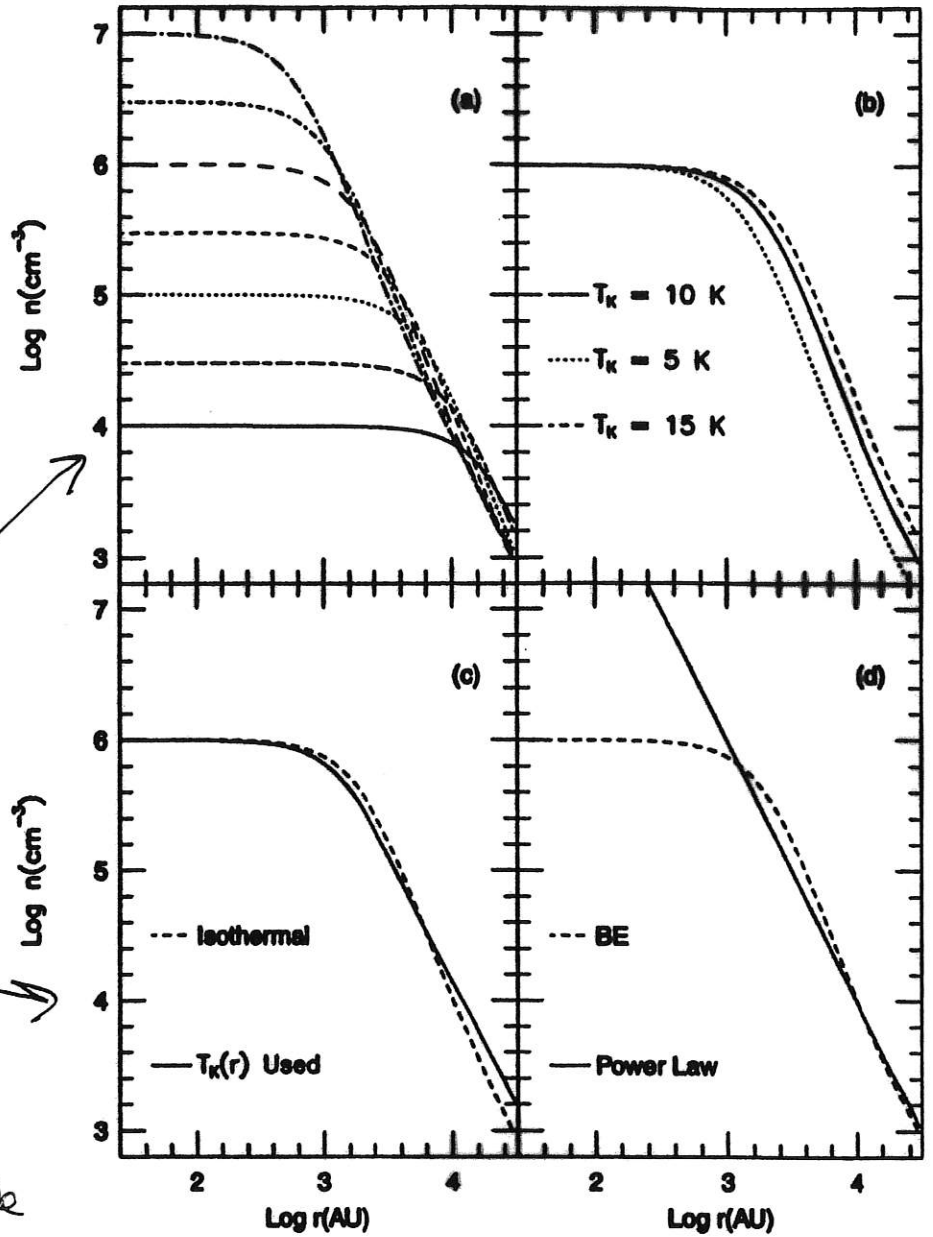
• modern dust opacities $K(\nu)$

FIG. 1.—Plots of log density vs. log radius in AU for the input physical models. In (a), Bonnor-Ebert spheres with constant kinetic temperature $T_K = 10$ K and central densities from $n_c = 1 \times 10^4$ to $n_c = 1 \times 10^7$ cm^{-3} are shown. In (b), Bonnor-Ebert spheres with $n_c = 1 \times 10^6$ cm^{-3} are shown for different, constant kinetic temperatures. In (c), a Bonnor-Ebert sphere with a variation in T_K based on iteration with the radiative transport code and assuming $T_K(r) = T_d(r)$ is compared to an isothermal ($T_K = 10$ K) Bonnor-Ebert sphere with the same n_c. In (d), a power law (PL2) corresponding to a singular isothermal sphere with $T_K = 10.4$ is compared to a Bonnor-Ebert sphere with $n_c = 1 \times 10^6$ cm^{-3}.

The resulting models:

adopt density
profiles for
various
Bonnor-Ebert
spheres $\longrightarrow$

← cores
are colder
on the inside
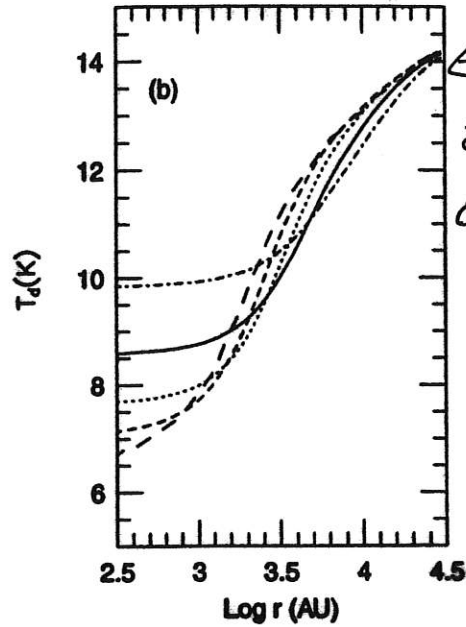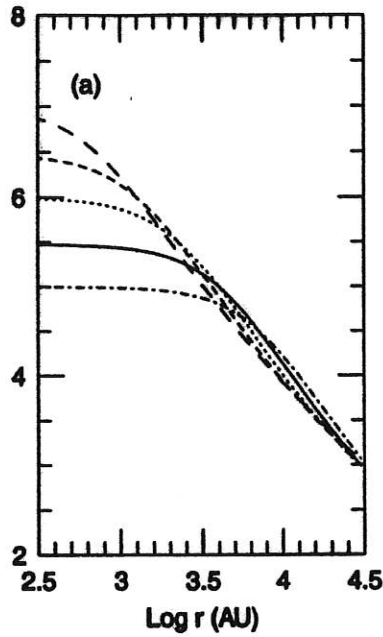
predicted
emission
profiles in
plane of the
sky $\longrightarrow$
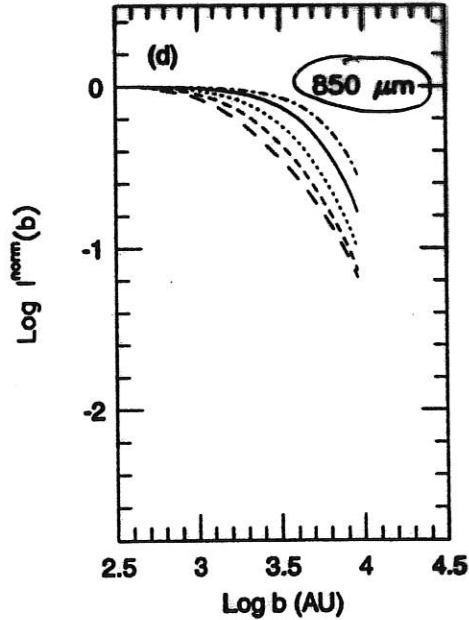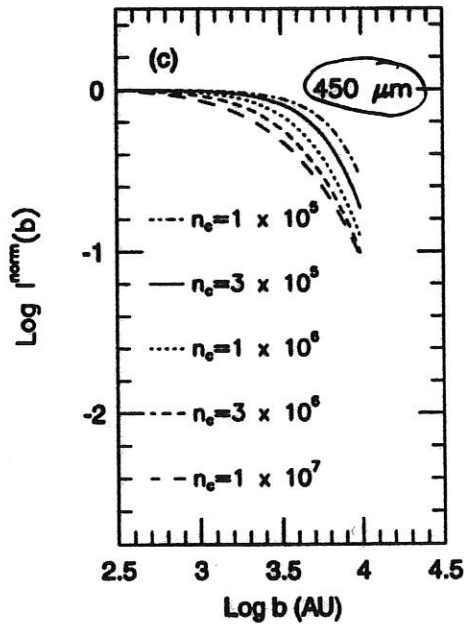
Evans et al.
2001

FIG. 4.—Density distributions for a series of Bonner-Ebert spheres are shown in (a). The resulting temperature distributions are shown in (b), with the same line coding; the densest models have the lowest central temperatures. In (c), the resulting intensity distributions at 450 μm are shown. In (d), the results for 850 μm are shown. The same line coding is used for all panels, with the densest models showing the fastest falloff with radius. The model emission in panels c and d has been convolved with the observed beam, and chopping by 120″ has been simulated, causing some of the drop around impact parameter b ~ 10,000 AU for a distance of 125 pc.
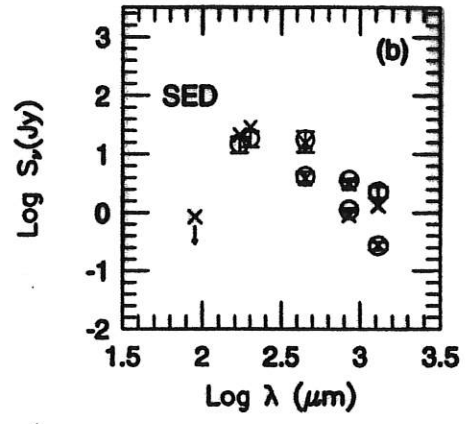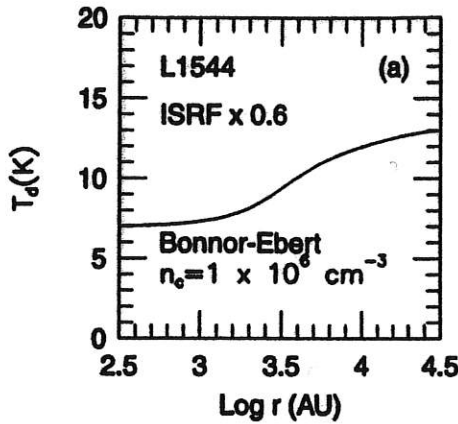
$\longrightarrow$ predicted intensity profiles include
known observational effects
  - beam shape
  - "chopping"

Model fits to the prestellar core £1544:

very cold →
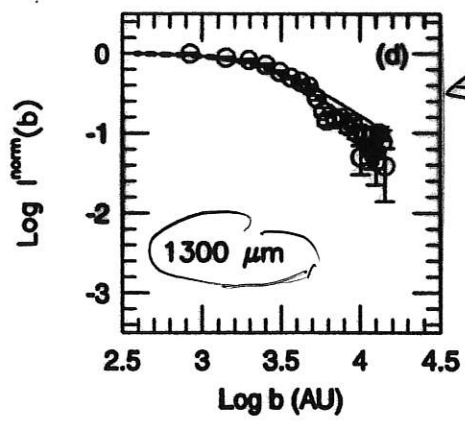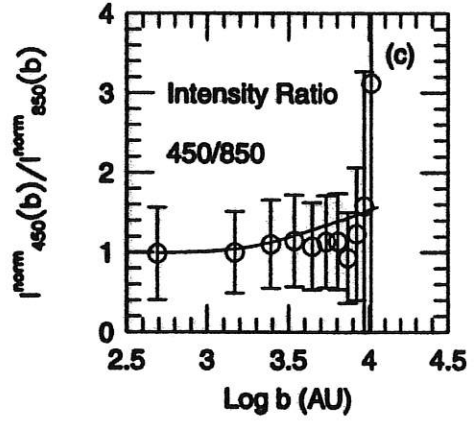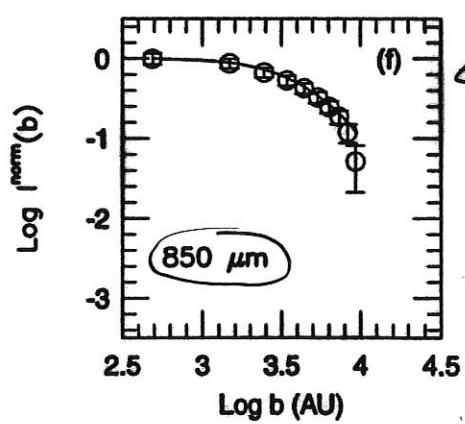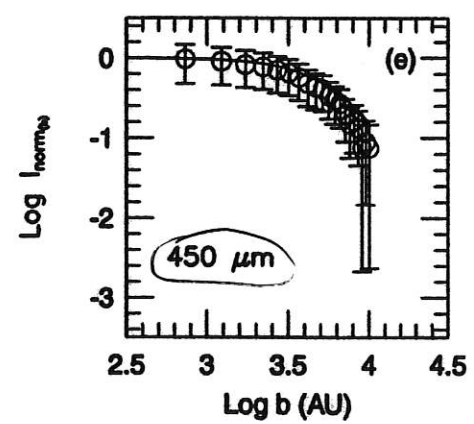on the
inside
→ 7 K!

EVANS ET AL. 2001

X = model
prediction

① = observation

data +
model →
(intensity ratio

data →
+model

FIG. 6.—Same as Fig. 5, but for L1544. The model is a Bonnor-Ebert sphere with $n_c = 1 \times 10^6$ cm^{-3} and a Black-Draine ISRF multiplied by 0.6. The 1300 μm data is from Ward-Thompson et al. (1999). At 140 pc, $b = 10^4$ AU corresponds to 71″.

note → radial profiles have been normalized
so center point ≡ 1
→ also have been radially averaged
(non-circular symmetry not included)

Also compare observations to power law
density profiles:

isothermal →

$n \propto r^{-2}$ and
$T = constant$
does not fit well

$T = T(r)$ →

BUT
$n \propto r^{-2}$ and
$T = T(r)$ via
radiative transfer
does fit the data
→ can't rule it
out for this
core
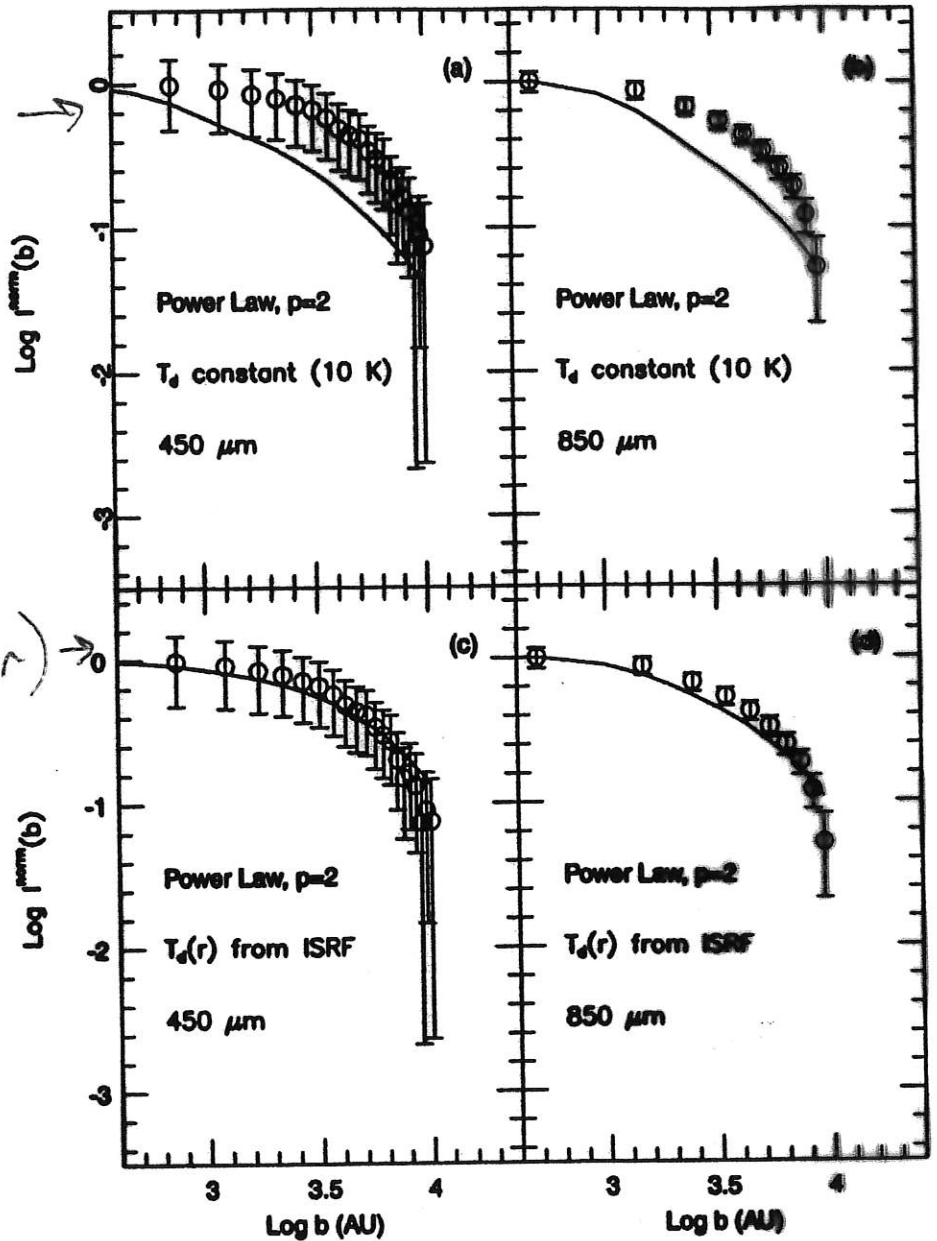

Fig. 7.—Normalized intensity distributions at 450 (a and c) and 850 (b and d) μm for a power-law density distribution, $n(r) = n(r_o)(r/r_o)^{-p}$, with $n(r_o) = 1.02 \times 10^5$, $p = 2$, and $r_o = 3 \times 10^4$ AU. The observations are of L1544. The top panels (a and b) show the model predictions with a constant $T_d(r) = 10$ K, while the bottom panels (c and d) show predictions for $T_d(r)$ calculated self-consistently with the radiative transport code, using the full Black-Draine ISRF.

Evans et al.
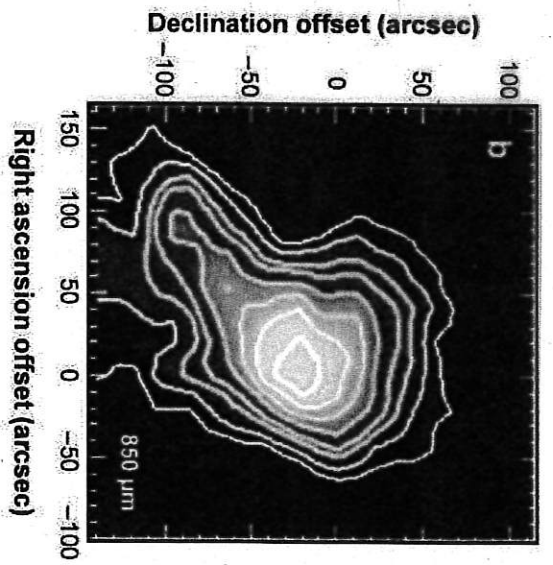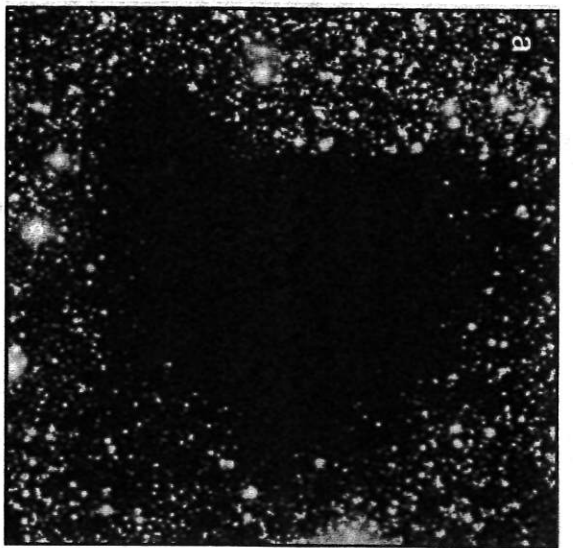2001

Astrochemistry in Cores

- observations of numerous cores in Taurus show larger sizes and linewidths for CS than for NH_3

- IR spectra show fundamental vibrational modes of solid-state H_2O, CO, CO_2
  - → ices contain a substantial fraction of O and C for $A_v > 3-7$ mag
  - → means CO doesn't trace H_2 well

- progress from using dust emission and/or extinction to map $N(H_2)$
  - → model for $n_{H_2}(r)$, $T_{dust}(r)$, $T_{gas}(r)$
  - → use these inputs + radiative transfer codes to constrain abundance profiles along line of sight

→ carbon-bearing molecules freeze-out onto grains much faster than nitrogen-hydrogen molecules
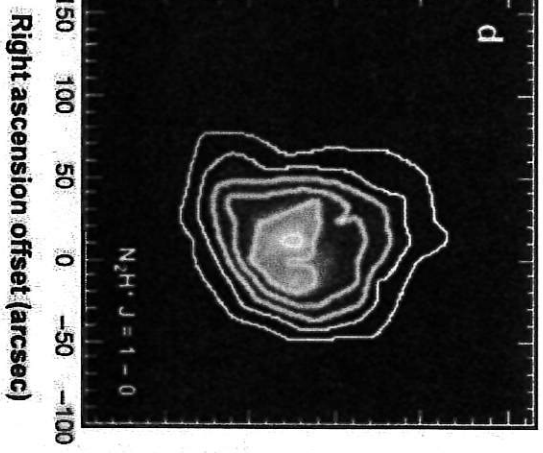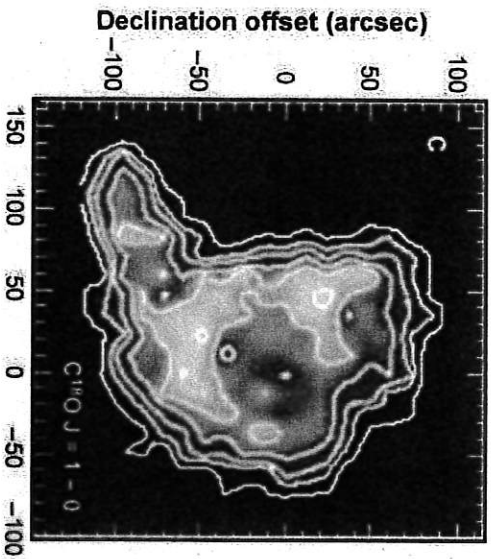
→ most CO frozen for $n_{H_2} > 10^5$ cm^{-3}

Freeze-out affects gas phase abundances

- H_2O frozen if $T_{dust} \lesssim 110 \, K$
  - $\rightarrow$ less O in gas phase $\therefore$ less H_2O, O_2
- CO is major destroyer of molecular ions
  - $\rightarrow$ removing CO from gas phase changes relative abundances of ions
    - especially H_3^+ $\rightarrow$ which forms N_2H^+
  - $\rightarrow$ without CO, more N_2H^+ survives
    - $\rightarrow$ also forms more NH_3
- N_2 likely major reservoir for nitrogen
  - $\rightarrow$ freezes out like CO
  - $\rightarrow$ but so much more abundant than N_2H^+, NH_3 that they can still form
- evolutionary timescale at $n \sim 10^4 \, cm^{-3}$
  - $\lesssim 0.5 - 1 \, Myr$
    - $\rightarrow$ otherwise CO depletion is too large

a

b

Declination offset (arcsec)

100   50   0   -50   -100

Right ascension offset (arcsec)

150   100   50   0   -50   -100

850 μm

c

Declination offset (arcsec)

-100   -50   0   50   100

Right ascension offset (arcsec)

150   100   50   0   -50   -100

C¹⁸O J = 1 - 0

d

Declination offset (arcsec)

-100   -50   0   50   100

Right ascension offset (arcsec)

150   100   50   0   -50   -100

N₂H⁺ J = 1 - 0

Left: Optical
extinction
right:N2H+ map

Left: C18O map

Right: 850
micron dust
emission map
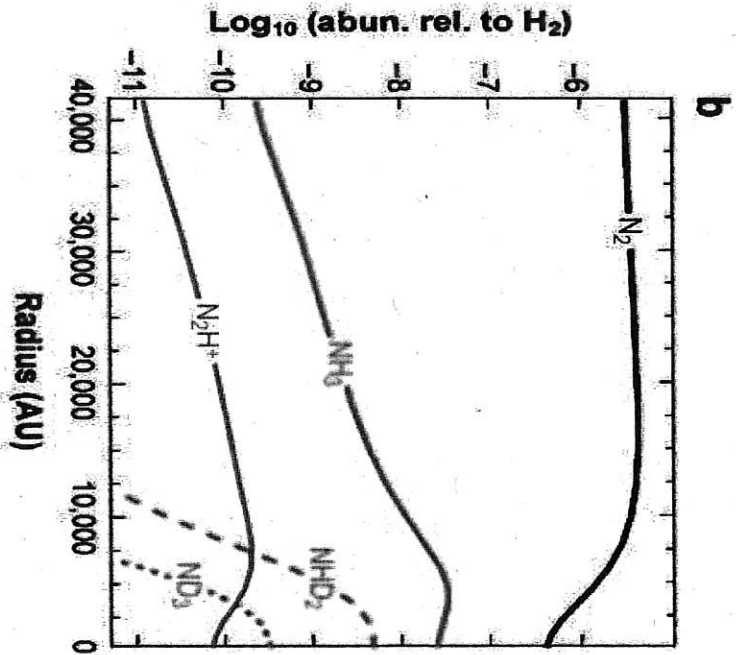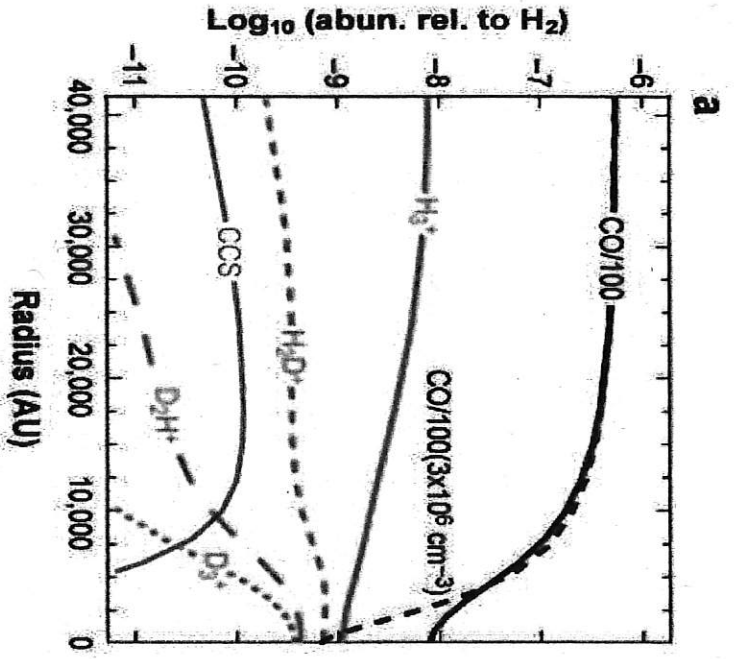
Bergin EA, Tafalla M. 2007.
Annu. Rev. Astron. Astrophys. 45:339-96

Figure 9: Plot of chemical abundances as a function of core depth for selected species from a chemical and dynamical model of a contracting Bonnor-Ebert sphere (taken from Aikawa et al. 2005). All species are shown at a timescale where n_H (center) = 3×10^5 cm^{-3}, excluding CO, which also is shown at n_H(center) = 3×10^6 cm^{-3}.